



Synthesis of Ni and Ni–Cu supported on carbon nanotubes for hydrogen and carbon production by catalytic decomposition of methane

Yi Shen^{a,b,*}, Aik Chong Lua^{b,**}

^a College of Light Industry and Food Sciences, South China University of Technology, Guangzhou, 510640, PR China

^b School of Mechanical and Aerospace Engineering, Nanyang Technological University, 50 Nanyang Avenue, 639798, Republic of Singapore

ARTICLE INFO

Article history:

Received 8 April 2014

Received in revised form 24 July 2014

Accepted 21 August 2014

Available online 28 August 2014

Keywords:

Hydrogen production

Catalytic decomposition of methane

Ni–Cu/CNT catalyst

Carbon morphology

ABSTRACT

Nickel and nickel–copper alloy supported on carbon nanotubes (CNTs) were examined as catalysts for hydrogen production by methane decomposition. The Ni/CNT and Ni–Cu/CNT catalysts were characterized using field emission scanning electron microscopy, energy dispersive X-ray microscopy, transmission electron microscopy and X-ray diffraction. The performance of the catalysts was dependent on the catalyst composition and reaction temperature. The Ni₇₈Cu₂₂/CNT catalyst exhibited the excellent catalytic performance with a stable methane conversion of 0.8 at 700 °C, a carbon yield rate of 0.08 g C/(min g Ni) at 743 °C and a carbon yield of 602 g C/g Ni at 700 °C. Carbon materials with various morphologies, i.e., herringbone carbon nanofibers (CNFs), platelet CNFs, bamboo-shaped CNFs, branched CNFs, multi-branched CNFs and onion-like carbons, depending on the catalyst composition and reaction temperature, were obtained. The morphology of the produced carbon material was correlated with the growth mechanism of the carbon material on the catalyst.

© 2014 Elsevier B.V. All rights reserved.

1. Introduction

Due to the great concern on global warming and energy supply security, renewable energy technologies are being extensively explored to reduce the emission of greenhouse gases and boost the global economic development. Being an efficient and environmentally friendly energy carrier, hydrogen can be utilized with high efficiency and zero emission of greenhouse gases and air pollutants. It has been widely accepted that hydrogen plays a critical role on sustainable energy future [1]. The production of hydrogen has attracted great attention from the scientific and industrial communities. For decades, steam reforming of natural gas has been the most widely used process for the industrial production of hydrogen. However, the production of hydrogen by this multi-step process results in high emissions of carbon dioxide and the end-product always contains some quantities of carbon monoxide, which prevents the resulting hydrogen being directly used in fuel

cells [2]. Alternatively, catalytic decomposition of methane (CDM) has been of great interest because only pure hydrogen and high quality carbon are obtained in this process [3–5]. CO_x-free hydrogen produced by CDM is favorable for fuel cell applications without further separation and purification processes. In addition, carbon is sequestered in the form of a stable valuable solid carbon nanotubes (CNTs) or carbon nanofibers (CNFs) rather than as a notorious greenhouse gas in the form of carbon dioxide. The feasibility of the CDM process is highly dependent on the efficiency and durability of the catalyst. The transition metals, i.e., Fe, Co and Ni show high catalytic activities due to their unique 3d-orbital properties. In particular, nickel has been the most widely studied as the active catalyst for the CDM. Considerable work has focused on the selection of catalyst support and the catalyst preparation [6–10]. Since the efficiency of nickel catalyst is thermodynamically limited by its deactivation temperature, many nickel-based alloys, i.e., Ni–Pt, Ni–Pd, Ni–Co, Ni–Mo and Ni–Cu were explored to improve the catalytic performance [11–15]. It was reported that Ni–Cu alloy catalysts prepared by the co-precipitation and impregnation methods exhibited enhanced catalytic activities [16–20]. However, it is still very challenging to achieve homogeneous dispersion and size control of catalyst particles [4]. In this work, we synthesized Ni/CNT and Ni–Cu/CNT catalysts by the polyol reduction method. To the best of authors' knowledge, this study is the first report on the catalytic

* Corresponding author at: College of Light Industry and Food Sciences, South China University of Technology, Guangzhou, 510640, PR China.
Tel.: +86 2087113843; fax: +86 2087113843.

** Corresponding author. Tel.: +65 67905535.

E-mail addresses: feyshen@scut.edu.cn (Y. Shen), maclua@ntu.edu.sg (A.C. Lua).

performance of Ni and Ni–Cu alloys obtained by the polyol reduction method. This simple one-pot synthesis method achieved homogeneous dispersion of catalyst particles on the CNT support with tunable size and composition. Unlike some hard-to-reduce oxide supports, e.g., SiO₂, Al₂O₃, CeO₂ and TiO₂, the selection of CNTs as catalyst supports has the advantages of preventing the generation of traceable carbon monoxide due to the reaction of the carbonaceous residues with the oxygen in the oxide supports and eliminating the etching process for the purification of the produced carbon materials [21]. Since CNTs are one of the products of the CDM process, the use of CNTs as catalyst support could further make this partially self-sustained CDM process more economical and feasible.

2. Experimental

2.1. Purification of multiwall carbon nanotubes

Multiwalled carbon nanotubes (MWCNTs, Shenzhen Nanotech Port Co. Ltd. China) were purified to remove the metallic catalyst. The details of the procedure are as follows: 1 g of MWCNTs was added into a 70 ml solution of concentrated nitric acid and sulfuric acid (volumetric ratio of 1:1). The MWCNTs were dispersed by ultrasonic for 30 min. The mixture was transferred into a 150 ml round flask and refluxed for 4 h at 120 °C under nitrogen atmosphere. After cooling to room temperature, the mixture was carefully filtered and rinsed with water several times. The purified MWCNTs were dried and ground for further use.

2.2. Sample preparation

The catalysts were synthesized using the polyol reduction method. Ethylene glycol was used as the solvent, reducing agent as well as protecting agent. The details of the procedure are as follows: 100 ml of ethylene glycol was introduced to a 150 ml beaker and 0.25 g of purified CNTs was dispersed into ethylene glycol by alternative ultrasonication and magnetic stirring. 1.2 g of sodium hydroxide and 5 mmol of metal precursors *i.e.*, nickel (II) nitrate hexahydrate and copper (II) nitrate trihydrate, with a given molar ratio was added into the mixture. After the complete dissolution of the precursors, 250 μ l of chloroplatinic acid solution (8 wt%) was also added into the mixture as the heterogeneous nucleation seed. Subsequently, the mixture was transferred into an oil bath and the reduction was carried out at 180 °C for 4 h under continuous magnetic stirring. After cooling to room temperature, the mixture was filtered and thoroughly washed with water and ethanol. The resulting catalyst was dried at 80 °C overnight using a vacuum oven. For convenience, the catalyst of pure nickel supported on CNTs was denoted as Ni/CNT and the catalysts of nickel–copper alloy supported on CNTs were denoted as Ni *x*–Cu *y*/CNT, where *x* and *y* are the atomic compositions of Ni and Cu, respectively.

2.3. Characterization of catalysts

A field emission scanning electron microscope (FESEM) (JSM-7600F, JEOL) and a transmission electron microscope (JSM2010, JEOL) were used to observe the morphology of the catalysts and the produced carbon materials. To analyze the crystalline structures of the catalysts, X-ray diffraction (XRD) patterns were recorded with a diffractometer (PW1830, Philips) equipped with Cu–K α radiation of 1.54 Å. The X-ray generator was set to be 40 kV and 40 mA. The value of *d* spacing was calculated from Bragg's law ($\lambda = 2d \sin \theta$). An energy dispersive X-ray (EDX) analyzer equipped in the FESEM was used to analyze the elemental composition of the samples.

The catalytic activities of the catalysts were tested with an experimental set-up [22,23]. In a typical process, a predetermined

amount of catalyst was loaded into the mid-section of a quartz tube reactor with an internal diameter of 10 mm and a length of 800 mm. The reactor was heated by an electric furnace with a temperature programmed controller (Carbonite 2416) and the temperature of the reactor was accurately monitored using a K-type thermocouple. The flow rates of the gases were measured and controlled by mass flowmeters (Alicat Scientific). Prior to the catalytic reaction, the system was flushed with nitrogen to remove the air. The concentrations of the outflow gases were analyzed by a calibrated gas chromatograph (Agilent 6890-5973 GC-MS network systems) equipped with a thermal conductivity detector. The methane conversion (χ) was calculated using following equation:

$$\chi = \frac{C_{H_2}}{C_{H_2} + 2C_{CH_4}}$$

where C_{H_2} and C_{CH_4} are the concentrations of hydrogen and methane in the outlet of the reactor, respectively, which were determined by GC–MS. Following the methane conversion, the carbon yield rate and hydrogen formation rate were calculated based on the reaction equation using the following relationship:

$$\text{Carbon yield rate} = \frac{1}{2} \text{ hydrogen formation rate} = \text{methane flowrate} \times \chi \text{ [unit: mol min}^{-1} \text{ g}_{NiCu}]$$

3. Results and discussion

3.1. Catalyst characterization

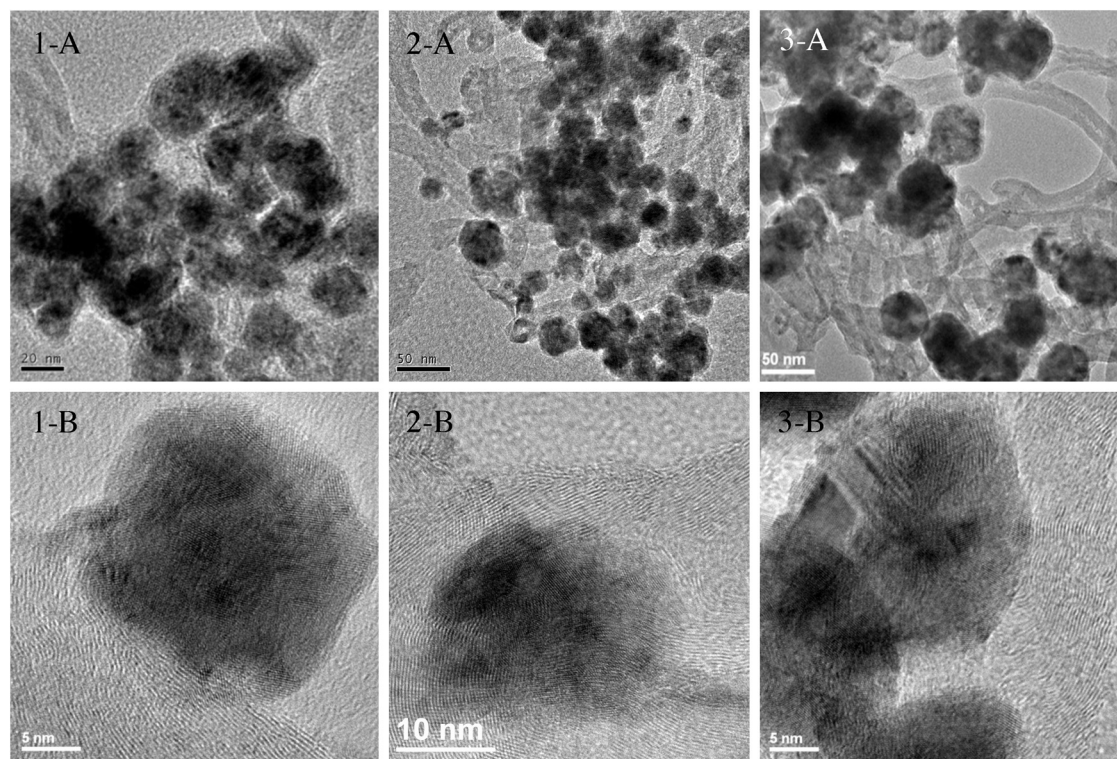
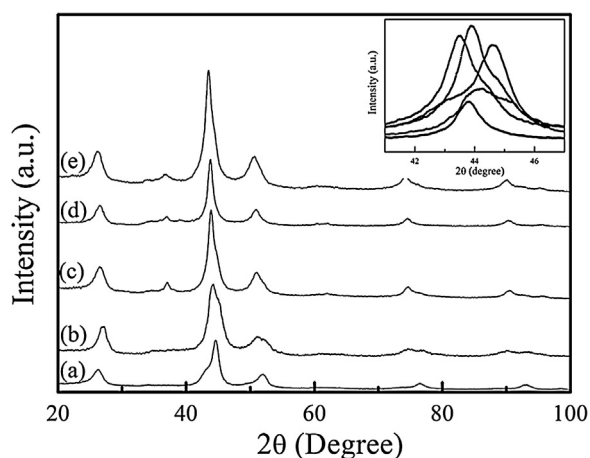
The actual atomic composition of the catalyst was determined from the EDX tests and the results are shown in Table 1. The actual ratios of nickel and copper in the catalysts were slightly lower than the nominal ratios in the feedstock. This could be related to the fact that copper ions are relatively easier to be reduced due to its higher standard reduction potential ($Cu^{2+} \rightarrow Cu^0 + 0.34 \text{ V}$) than that of Ni^{2+} ($Ni^{2+} \rightarrow Ni^0 - 0.26 \text{ V}$), resulting in the segregation of copper in the cores of the particles. Oxygen atoms were detected by the EDX tests. This could be attributed to the presence of metal oxides due to the surface oxidation of the metal atoms. The morphology of the catalyst was characterized by FESEM as shown in Fig. S1 (see the supporting information). The catalyst consisted of quasi-spherical particles uniformly dispersed into the CNT support matrix. No large particle aggregate was observed in the catalysts, indicating that the CNT support could effectively stabilize the active metal particles. The morphology of the catalyst was further examined by TEM as shown in Fig. 1. It could be seen that all the particles were closely adhered to the CNTs and that no isolated particle was observed despite the long duration of ultrasonication during the sample preparation process. The interaction between the particles and CNTs was further revealed by the high-resolution TEM (HRTEM) micrographs as shown in Figs. 1–3B. The lattice fringes of CNTs and particles were interweaved in the interfaces. The HRTEM micrographs also indicated that the particles were polycrystalline. Due to surface oxidation, two distinct lattice fringes with spacings of 2.0 and 2.4 Å, which could be assigned to the *d*-spacing values of Ni–Cu (1 1 1) and NiO (1 0 1), respectively, were observed in the particle as shown in Fig. 2S (see the supporting information). The size distribution of the particles in the catalysts was determined based on the TEM micrographs as shown in Table 1 and Fig. 3S (see the supporting information). The pure Ni particles in the Ni–CNT catalysts had an average diameter of *ca.* 22 nm. With increasing copper content in the catalysts, the size of the Ni–Cu alloy particles increased from 25 nm in the Ni₈₃Cu₁₇–CNT catalyst to 42 nm in the Ni₄₇Cu₅₃–CNT catalyst.

Fig. 2 shows the XRD patterns of the catalysts. The peak located at around 26° was attributed to the graphitic (0 0 2) diffraction of the CNT support. Four distinct diffraction peaks at $2\theta = 44.4, 51.9,$

Table 1

Atomic composition, particle sizes, and crystallographic properties of Ni/CNT and Ni–Cu/CNT catalysts.

Sample	Nominal Ni:Cu ratio	Actual Ni:Cu ratio ^a	Particle size (nm) ^b	NiCu (111) position (deg)	Lattice parameter (Å) ^c	Crystal size (Å) ^d
A	100Ni	100Ni	22	44.4	3.53	51
B	90:10	87:13	25	44.1	3.55	29
C	80:20	78:22	31	43.9	3.57	39
D	60:40	58:42	35	43.8	3.58	55
E	50:50	47:53	42	43.6	3.59	74

^a Determined from the EDX results, for each sample, five tests were carried out and the average values were calculated.^b Determined based on TEM micrographs, for each sample, 100 particles were averaged.^c Calculated based on the face-centered cubic structure of Ni crystal.^d Determined from XRD patterns based on Scherrer equation.**Fig. 1.** TEM micrographs of (1) Ni-CNT, (2) Ni₈₇–Cu₁₃/CNT, (3) Ni₄₇–Cu₅₃/CNT catalyst: (A) low magnification and (B) high magnification.**Fig. 2.** XRD patterns of (a) Ni/CNT, (b) Ni₈₇–Cu₁₃/CNT, (c) Ni₇₈–Cu₂₂/CNT, (d) Ni₅₈–Cu₄₂/CNT, and (e) Ni₄₇–Cu₅₃/CNT catalyst.

76.1 and 92.6° were also observed from the XRD patterns of the Ni-CNT catalyst which could be indexed to metallic Ni planes (1 1 1), (2 0 0), (2 2 0) and (3 1 1), respectively, (JCPDS #04-0850). In the bimetallic catalyst samples, Ni–Cu alloy was formed as evidenced

by the downward shifts in the position of the metallic Ni peaks, e.g., the Ni (1 1 1) diffraction peak shifted from 44.4° to 43.6° with increasing copper content in the catalyst (see inset in Fig. 2). The peak located at 37° could be attributed to the presence of metal oxides in the metallic particles due to the surface oxidation as confirmed by the HRTEM micrograph (Fig. 2S, see the supporting information). The lattice parameters and crystal sizes of the Ni and Ni–Cu alloys were calculated based on the XRD patterns as shown in Table 1. With increasing copper content, the lattice parameters of the metal particles increased from 3.53 Å to 3.59 Å. The Ni and Ni–Cu crystal sizes were calculated using the Scherrer equation based on the (1 1 1) diffraction. The pure Ni particles had a crystal size of 51 Å. The introduction of copper initially decreased the crystal size and further increases in copper content led to increasing crystal sizes of Ni–Cu alloy particles.

3.2. Catalytic results

Fig. 3 shows the carbon yield rates and hydrogen formation rates of the catalysts as a function of temperature. The carbon yield rates of the catalysts initially increased with increasing reaction temperature due to the endothermic property of the CDM reaction. It then decreased with further increases in temperature due to catalyst deactivation. The Ni-CNT catalyst achieved a maximum

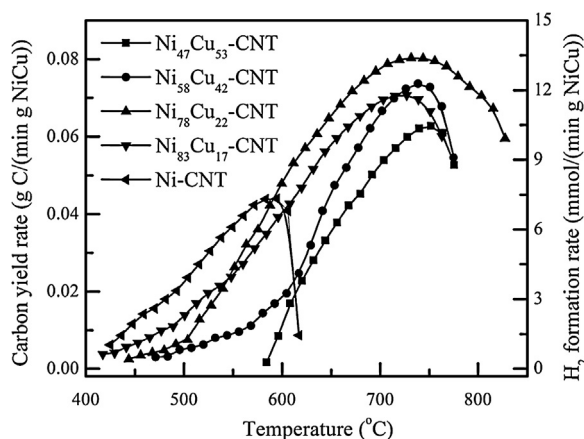


Fig. 3. Carbon yield rates of the catalysts as a function of temperature. (Experimental conditions: CH₄:N₂ = 3:5, total flow rate = 20 ml min⁻¹; catalysts mass: 40–45 mg.)

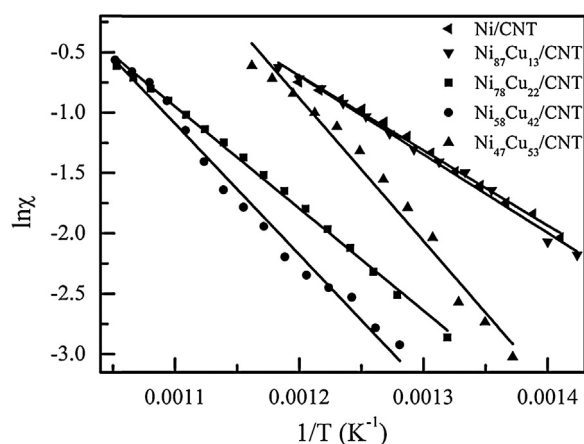


Fig. 4. Arrhenius plot for the catalysts.

carbon yield rate of 0.044 g C/(min g Ni) at 595 °C, corresponding to a hydrogen formation rate of 7.4 mmol min⁻¹ g_{NiCu}. With the introduction of copper, the carbon yield rates and hydrogen formation rates of the Ni–Cu based catalysts decreased at lower temperatures (when the temperature was less than 550 °C) as compared with those of Ni–CNT catalyst. However, the maximum carbon yield rates and hydrogen rates of the catalysts significantly increased, *i.e.*, the Ni₈₃Cu₁₇-CNT, Ni₇₈Cu₂₂-CNT, Ni₅₈Cu₄₂-CNT and Ni₄₇Cu₅₃-CNT catalysts exhibited maximum carbon yield rates of 0.071, 0.08, 0.074 and 0.063 g C/(min g NiCu) at 727, 743, 739 and 752 °C, respectively. To further investigate the effects of copper on the catalytic activities of the catalysts, the activation energy (*E_a*) of methane decomposition on the catalyst was determined based on the Arrhenius equation as shown in Fig. 4. The Ni–CNT catalyst had an *E_a* value of 52 kJ/mol, which was slightly higher than that of Ni–Al₂O₃ catalyst (46 kJ/mol) as reported by Avdeeva *et al.* due to the change in catalyst support [15]. The Ni–Cu based catalysts possessed higher *E_a* values as compared with that of the Ni–CNT catalyst. With increasing copper content, the *E_a* values of the Ni–Cu based catalysts increased from 54 kJ/mol to 99 kJ/mol, which was consistent with the results obtained from the Ni–Cu/Al₂O₃ catalysts as reported by Reshetenko *et al.* [24].

To further characterize the catalytic activities of the catalysts, the conversions of methane on the catalysts were recorded as shown in Figs. 5 and 6. The Ni–CNT catalyst had stable methane conversion values of 0.31, 0.45 and 0.48, at 500, 550 and 575 °C. The methane conversion increased to 0.54 at 600 °C, but decreased sharply with increasing reaction time as shown in Fig. 6. The

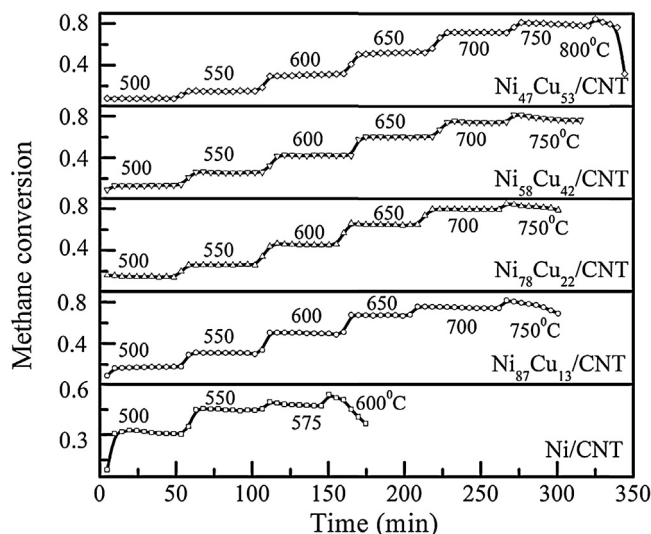


Fig. 5. Methane conversion on the catalysts at stepwise heating temperatures. The numbers shown in the graph refer to the corresponding step temperature. (10 mg of metallic nickel was involved for all the catalyst samples, CH₄:N₂ = 3:5, total flow rate = 20 ml min⁻¹.)

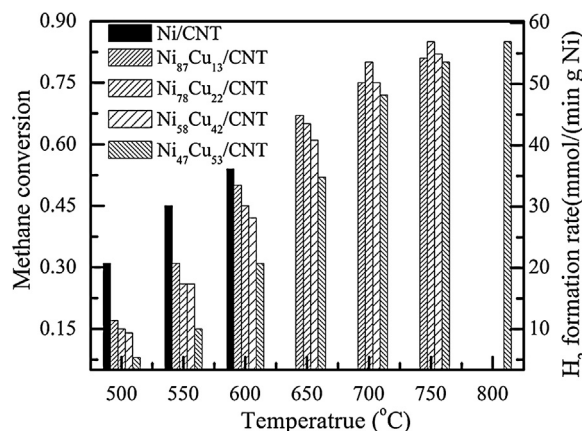


Fig. 6. Methane conversion of the catalyst at various temperature stages determined from a stepwise heating mode (The methane conversion values of Ni/CNT at 575 °C and of Ni₄₇Cu₅₃/CNT at 800 °C were not included in this figure).

optimum reaction temperature of the Ni–CNT catalyst was estimated to be 575 °C, which was higher than that of non-supported Ni catalyst (550 °C) as reported by Wang and Lua [22]. This could be attributed to the favorable stabilizing effects of CNT support on the active Ni particles. With the introduction of copper, the Ni–Cu based catalysts exhibited lower methane conversion values at low temperatures, *i.e.*, the methane conversion values were 0.17, 0.15, 0.14 and 0.08 at 500 °C for the Ni₈₃Cu₁₇-CNT, Ni₇₈Cu₂₂-CNT, Ni₅₈Cu₄₂-CNT and Ni₄₇Cu₅₃-CNT catalyst, respectively. However, the optimum reaction temperatures and the maximum methane conversion values of the Ni–Cu based catalysts were significantly increased. The Ni₈₃Cu₁₇-CNT, Ni₇₈Cu₂₂-CNT, Ni₅₈Cu₄₂-CNT catalysts exhibited stable methane conversion values of 0.75, 0.8 and 0.75, respectively, at 700 °C while the Ni₄₇Cu₅₃-CNT catalyst achieved a stable methane conversion value of 0.8 at 750 °C.

Ni–Cu alloys were extensively studied as catalysts for the CDM process. It has been accepted that the growth of CNFs on the catalyst particles is based on the adsorption–diffusion–precipitation mechanism [25]. The methane molecules first adsorb and dissociate on the metal surface to form carbon atoms. The carbon species diffuse through the metal particle and precipitate at the rear side of

Table 2

Methane conversion, activation energy and carbon yield of the resulting catalyst. For the Ni-CNT sample, the decomposition reaction was carried out at 575 °C while for the Ni-Cu alloy based catalysts the reactions were carried out at 700 °C to determine the carbon yield values.

Sample	Activation energy (kJ/mol) ^a	Carbon yield (g C/g Ni) ^b	Carbon yield (g C/g Ni) ^c
Ni/CNT	52	377	358
Ni ₈₇ Cu ₁₃ /CNT	54	503	496
Ni ₇₈ Cu ₂₂ /CNT	70	614	602
Ni ₅₈ Cu ₄₂ /CNT	90	529	506
Ni ₄₇ Cu ₅₃ /CNT	99	415	407

^a Determined from Arrhenius equation by plotting $\ln \xi \sim 1/T$, where ξ and T are the methane conversion value and the corresponding temperature, respectively.

^b Theoretical carbon yield values calculated by integrating.

^c Carbon yield values determined by measuring the samples before and after the reactions.

the particle to form CNFs. The actions of dissociation and diffusion play a critical role and a balance between the dissociation rate and diffusion rate has to be achieved to maintain continuous growth of CNFs. Copper with a full-filled 3d orbital is not active for methane dissociation but the presence of copper could significantly affect the electronic and surface properties of nickel [26]. At lower reaction temperatures, since copper is less active for methane dissociation, the presence of copper atoms in the Ni-Cu alloy surface reduced the number of active sites, resulting in lower dissociation rates. In addition, copper is relatively rich with d electrons, the introduction of copper could exert electronic effects on nickel atoms. Consequently, compared with the Ni/CNT catalyst, the Ni-Cu based catalysts exhibited lower methane conversions at lower temperatures as shown in Figs. 3 and 5. The effects of copper on methane decomposition were also indicated by the increase in E_a values of Ni-Cu based catalysts as shown in Fig. 4 and Table 2. At temperatures above 600 °C, the pure nickel catalyst was deactivated due to the fact that the methane dissociation rate was faster than carbon diffusion rate, resulting in encapsulation of nickel particles by graphitic layers. Under this circumstance, the presence of copper could modulate the dissociation rate as well as increase the carbon diffusion rate due to the increase in the lattice parameter of Ni-Cu crystals as indicated by the XRD results (see Table 1). The balance between methane dissociation and carbon diffusion was restored and subsequently the continuous growth of CNFs maintained.

To study the life span of the catalyst, the reaction was carried out in a fixed temperature using pure methane until the complete deactivation of the catalyst (when methane conversion was less than 5%) and these methane conversion curves *versus* time for all the catalysts tested are shown in Fig. 7. The Ni-CNT catalyst possessed a life span of 1630 min at 575 °C while the Ni₈₃Cu₁₇-CNT, Ni₇₈Cu₂₂-CNT, Ni₅₈Cu₄₂-CNT and Ni₄₇Cu₅₃-CNT catalysts exhibited life spans of 1740, 1860, 1760 and 1580 min, at 700 °C, respectively. The evolution curve of the Ni-CNT catalyst consisted of three steps, *i.e.*, induction stage (not shown), plateau stage and deactivation stage, which was in agreement with the results reported by Avdeeva et al. [15]. In contrast, the methane conversion curve of the Ni-Cu based catalysts showed a wave plateau pattern for the initial 300 min, followed by a short plateau stage and a deactivation stage. This behavior could be related to the changes in the atomic composition on the surface of Ni-Cu alloy particles during the reaction. It was reported that the assembly of copper atoms in Ni (1 1 1) planes at high temperatures in a so-called “geometry effect” could provide more precipitation sites for CNF formation [20]. The carbon yield of the catalyst was theoretically calculated from the data in Fig. 7 and was experimentally determined from the weight difference between the pristine catalyst and the deactivated catalyst. The experimental carbon yields of the catalysts were very

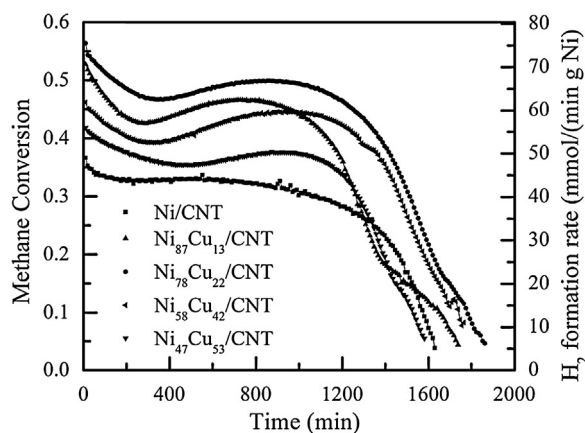


Fig. 7. Kinetic curves of methane conversion over the catalysts during the decomposition reaction (5 mg of metallic nickel was involved for all the catalyst samples; pure methane, volume flow rate = 7.5 ml min⁻¹). For the Ni-CNT sample, the reaction was carried out at 575 °C while for the Ni-Cu alloyed catalysts the reactions were carried out at 700 °C.

close to the theoretical values as shown in Table 2. The Ni-CNT catalyst had a carbon yield of 358 g C per g of Ni at 575 °C, which was higher than the maximum value of 302 g C per g of Ni obtained from the unsupported Ni catalyst reported by Wang and Lua [22]. Compared with the Ni-CNT catalyst, the Ni-Cu based catalyst exhibited higher carbon yields. Carbon yields of 496, 602, 506 and 407 g C per g of Ni were obtained from the Ni₈₃Cu₁₇-CNT, Ni₇₈Cu₂₂-CNT, Ni₅₈Cu₄₂-CNT and Ni₄₇Cu₅₃-CNT catalysts at 700 °C, respectively. The maximum carbon yield of 602 g C per g of Ni achieved from the Ni₇₈Cu₂₂-CNT catalyst was much higher than the value of 465 g C per g of Ni obtained from the 15Ni-3Cu-2Al catalyst reported by Chen et al. [27]. It should be noted that the carbon yield of the catalyst can be further enhanced by optimization of the reaction process.

3.3. Carbon morphology

Apart from the methane conversion and carbon yield, another important aspect of the CDM process is to control the morphology and structure of the produced carbon material. Fig. 8A shows the CNFs obtained from the Ni/CNT catalyst at 550 °C. Several CNT supports with smaller diameters were also observed in the micrograph as indicated by the arrows. Fig. 8B shows a typical CNF obtained from the Ni-CNT catalyst. The resulting CNF exhibited a herringbone structure with diameters of *ca.* 40 nm and wall thicknesses of *ca.* 15 nm. Fig. 8B shows a typical conical crystalline Ni particle located on the tip of a CNF, indicating the tip-based growth mechanism. The pear-like Ni particle had a larger particle size than that of the pristine Ni particle, indicating the occurrence of coalescence and reshaping of Ni particles during the CDM process. The interface between the Ni particle and CNF showed that the graphene layers were properly curved to match the lattice of Ni (1 1 1) planes, resulting in a strained quasi-coherent interface as indicated by the local darkness of the Ni lattice as shown in Fig. 8D and E [28]. Careful inspection could reveal that many steps were present at the Ni surface. A graphene layer was sprouted from each of these step edges. It was reported that the Ni step edges were formed during the initial stage of the reaction and that these step edges played a key role in the nucleation and growth of graphene sheets [29]. Carbon atoms continuously diffused towards the interface and preferentially nucleated at the step edges while Ni atoms diffused towards the free Ni surface, resulting in the periodic elongation-contraction process during the growth of CNFs as observed by Helveg et al. [30].

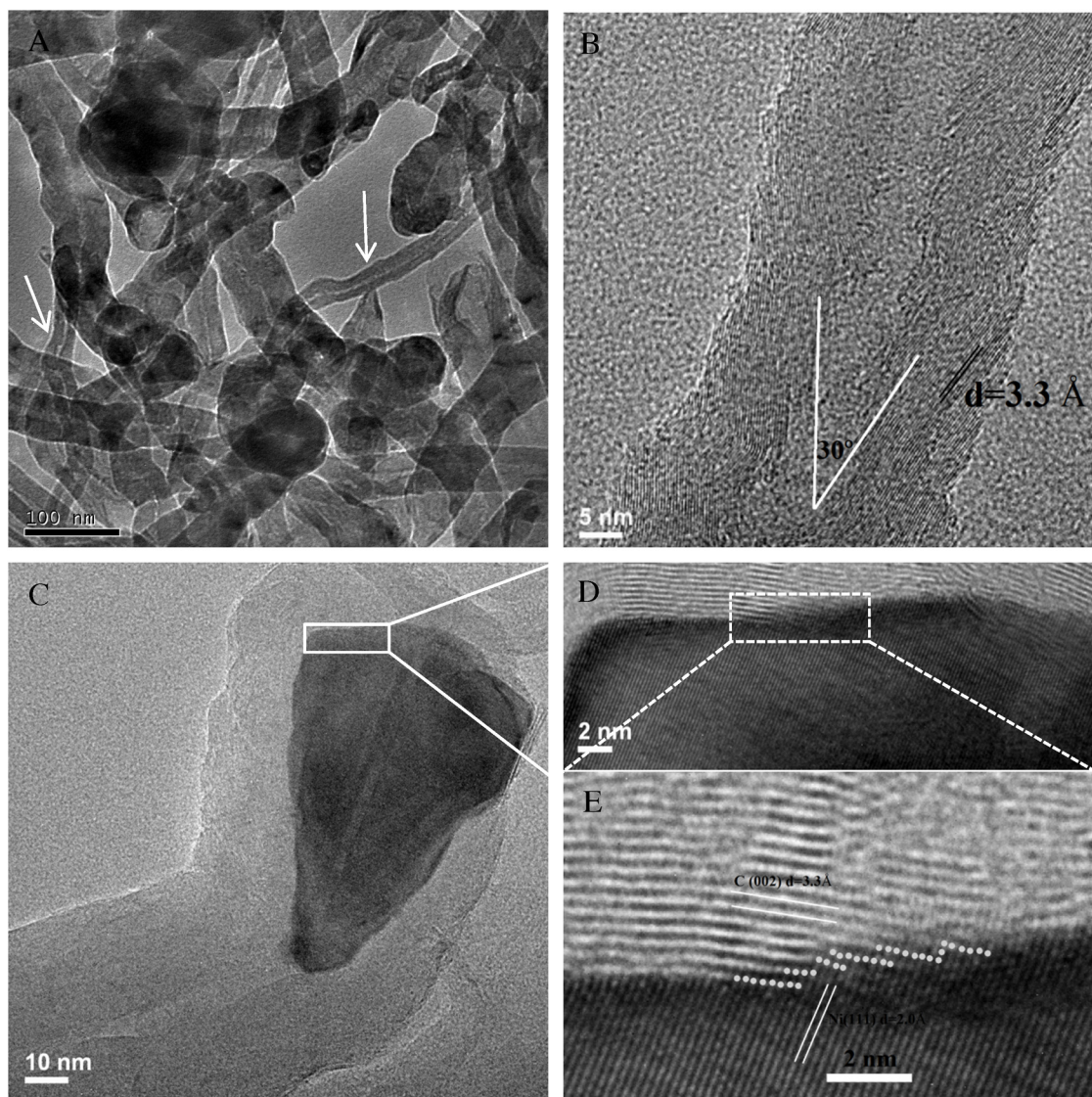


Fig. 8. TEM micrographs of the herringbone CNFs obtained from Ni/CNT catalyst at 550 °C. (A) Overview of the CNFs, (B) a typical herringbone CNF, (C) a typical herringbone CNF grown from a concave Ni particle, (D) magnification of the marked region in (C) and (E) further magnification of the marked region in (D).

Fig. 9 shows typical bamboo-shaped CNFs obtained from the Ni₄₇Cu₅₃/CNT catalyst at 750 °C. The bamboo-shaped CNFs consisted of many uniformly-sized hollow compartments which were separated by transversely extended graphene layers as shown in Fig. 9. The wall of each compartment consisted of oblique graphene layers with respect to the fiber axis. The Ni–Cu alloy particle also exhibited an elongated conical shape which was closely surrounded by graphitic layers as shown in Fig. 9B. The lattice fringe with a spacing of 0.21 nm could be assigned to the d-spacing values of Ni–Cu (111), which was parallel to the graphitic (002) lattice fringe with a spacing of 0.34 nm. Isolated dangling graphene sheets were observed near the knot of the bamboo-shaped CNF as indicated by the arrow in Fig. 9B. It should be noted that bamboo-shaped CNFs were exclusively obtained from the Ni–Cu based catalysts at higher temperatures (>700 °C) in this study. The high copper content in the catalyst was favorable for the growth of bamboo-shaped CNFs. This could be explained from the effects of copper doping on the physico-chemical properties of the catalyst. Copper has a lower melting point of 1083 °C as compared to 1453 °C for nickel. The presence of copper in the catalyst is necessary to achieve a quasi-liquid

state of Ni–Cu alloy particles at the reaction temperatures. It was suggested that the catalyst particle exhibited a quasi-liquid state. Two distinct movements of the catalyst particle, *i.e.*, elongation and contraction, with respect to the CNF, were involved during the growth of bamboo-shaped CNFs [31]. The elongation movement was driven by the alignment of graphene layers at the carbon–metal interface and the accumulated interfacial force led to the contraction of the metal particle. Moreover, the increases in copper content in Ni–Cu particles could significantly enhance the deformability and the metal–carbon interfacial wettability. For example, Helveg et al. reported a length–width ratio of *ca.* 4 for the elongated nickel particles during the growth of the CNFs [30]. Comparatively, much larger length–width ratios (up to 20) were observed for the elongated Ni–Cu particles in this study as shown in Fig. S4 (see the supporting information). It could be deduced that elongation of Ni–Cu particle would maintain for a longer time as compared with that of the nickel particle (less than 0.5 s as reported by Helveg et al. [30]) before contraction. During this period, a hemispherical cap would be formed around the tip of the catalyst particle, resulting in formation of bamboo knot. The time gap between the elongation and contraction would play a critical role in the formation of

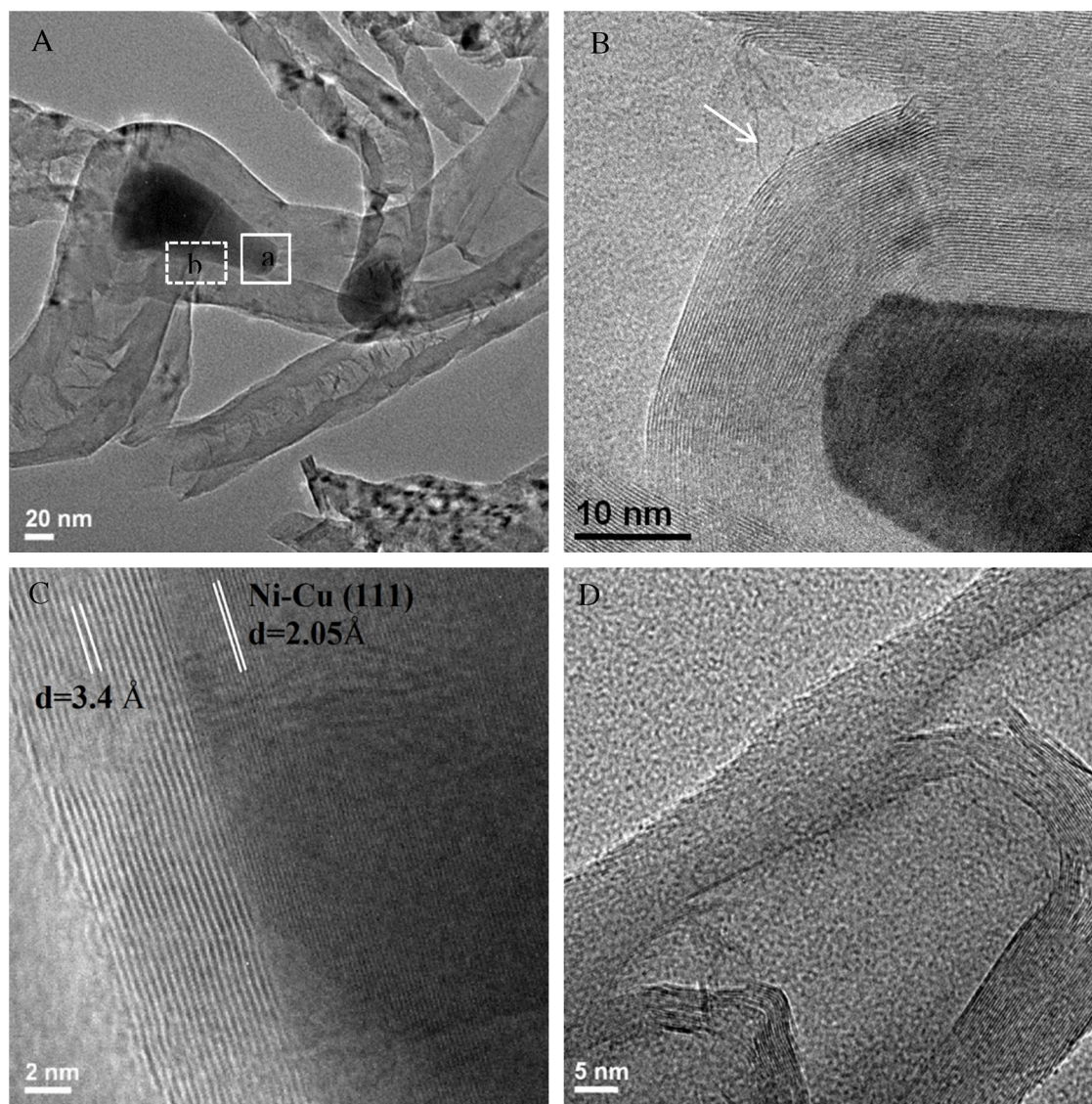


Fig. 9. TEM micrographs of the bamboo-shaped CNFs obtained from the $\text{Ni}_{47}\text{Cu}_{53}/\text{CNT}$ catalyst at 750°C . (A) Overview of the bamboo-shaped CNFs, (B) magnification of the region marked “a” in (A), (C) magnification of the region marked “b” in (A) and (D) a typical bamboo-shaped CNF.

bamboo-shaped CNFs. It was confirmed by Lin et al. that formation of a full complete hemispherical cap prior to the contraction of the catalyst particle resulted in a complete knot whereas a partial formation of the hemispherical cap led to an incomplete knot [32]. The presence of the dangling graphene sheet could be exactly due to the incomplete growth of the graphene sheet which failed to bridge the walls of the bamboo-shaped CNF.

Fig. 10 shows typical branched CNFs obtained from the $\text{Ni}_{78}\text{Cu}_{22}/\text{CNT}$ catalyst using a stepwise heating mode. Two carbon filaments grew from an elongated particle with a length of several hundreds of nanometers as shown in Fig. 10A. HRTEM micrographs indicated that the graphitic layers in the branch were curved to form a bow-like structure and that the graphitic layers in the stem were almost parallel to the axis of the fiber (similar to CNTs) as shown in Fig. 10C. Based on the bending direction of the graphitic layers as shown in Fig. 10D, the growth direction of the fiber could be determined as shown in Fig. 10A. It should be noted that no branched CNFs were observed from the Ni/CNT catalyst. The growth of branched CNFs was preferentially observed from the Ni-Cu based catalysts using a stepwise heating mode as discussed in Fig. 5. Similar to the bamboo-shaped CNFs, the formation of the branched CNFs

could also be related to the quasi-liquid state of the Ni-Cu alloy particles. It was proposed that formation of branched CNFs could be due to the change in the orientation of the catalyst particle and the distribution of the carbon atoms on the catalyst because of the fluctuations in temperature, gas flow or carbon source supply [33,34]. In this study, the fluctuation could be attributed to the temperature variations during the stepwise heating process.

Multi-branched CNFs were observed from the Ni-Cu based catalysts at lower reaction temperatures ($550\text{--}600^\circ\text{C}$) as shown in Fig. S5A. Several carbon filaments sprout from one large faceted Ni-Cu particle to form an octopus structure as reported by Ermakova et al. [35]. Each branch exhibited the so-called platelet structure, which consisted of a stack of graphene layers, perpendicular to the fiber axis (see Fig. S5B). The formation of the octopus structure was due to the copper segregation on Ni-Cu alloy (111) planes, which facilitated the multi-directional growth of CNFs as reported by Monthieux et al. [36]. Fig. S5C shows the TEM micrographs of an onion-like carbon obtained from the $\text{Ni}_{58}\text{Cu}_{42}/\text{CNT}$ catalyst at 700°C . The carbon nanoonion (CNO) consisted of a core of catalyst particle wrapped by curved graphitic layers. The catalyst particle exhibited an irregular spherical shape which was

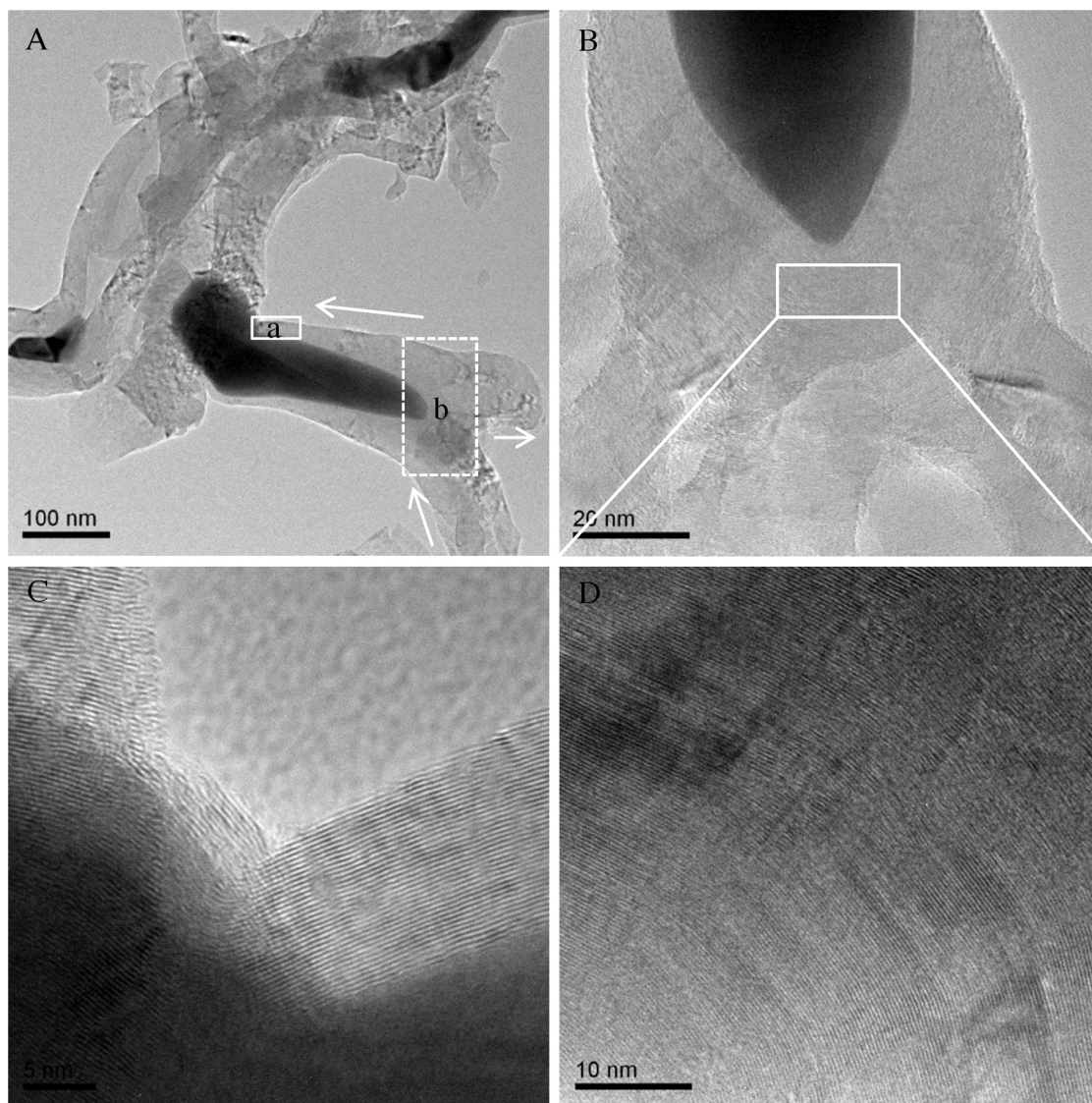


Fig. 10. TEM micrographs of the branched CNFs obtained from the $\text{Ni}_{78}\text{Cu}_{22}/\text{CNT}$ catalyst using a stepwise heating mode. (A) Overview of the branched CNFs, (B) magnification of the region marked “b” in (A), (C) magnification of the region marked “a” in (A) and (D) magnification of the marked region in (B).

very similar to that of pristine Ni–Cu alloy particles, indicating that the elongation or faceting of the catalyst particle as observed in the former cases did not occur. The formation of the CNO could probably be closely related to the fact that the catalyst particle failed to reshape during the initial stage of the reaction, preventing the elongation–contraction scenario from happening. The carbon atoms deposited uniformly on the isotropic catalyst particle, resulting in the formation of CNOs. The yield of the CNOs is very limited due to the fast deactivation of the catalyst particles.

4. Conclusions

Ni and Ni–Cu alloys with various atomic ratios supported on CNTs were synthesized by the polyol reduction method. It was found that CNTs were an effective support for stabilizing the Ni and Ni–Cu particles. The resulting catalysts exhibited extremely high activities for the CDM. The introduction of copper in the catalysts greatly enhanced the optimum reaction temperature, resulting in higher methane conversions and carbon yields. The methane conversions, carbon yield rates and carbon yields of the catalysts were

highly dependent the composition of the catalyst and reaction temperature. The Ni/CNT catalysts had a stable methane conversion of 0.48 at 575 °C, a maximum carbon yield rate of 0.044 g C/(min g Ni) at 595 °C and a carbon yield of 358 g C/g Ni at 575 °C. The $\text{Ni}_{78}\text{Cu}_{22}/\text{CNT}$ catalyst had a stable conversion rate of 0.8 at 700 °C, a maximum carbon yield rate of 0.08 g C/(min g Ni) at 743 °C and a carbon yield of 602 g C/g Ni at 700 °C. The Ni/CNT catalyst produced herringbone CNFs while the Ni–Cu based catalysts produced various carbon materials including bamboo-shaped CNFs, branched CNFs, multi-branched CNFs and CNOs, depending on the catalyst composition and reaction temperature. It was demonstrated that the introduction of copper significantly affected the physicochemical properties of the catalyst and the formation mechanisms of carbon materials.

Appendix A. Supplementary data

Supplementary data associated with this article can be found, in the online version, at <http://dx.doi.org/10.1016/j.apcatb.2014.08.038>.

References

- [1] M. Balat, *Int. J. Hydrog. Energy* 33 (2008) 4013–4029.
- [2] J. Sun, X.P. Qiu, F. Wu, W.T. Zhu, *Int. J. Hydrog. Energy* 30 (2005) 437–445.
- [3] H.F. Abbas, W.M.A.W. Daud, *Int. J. Hydrog. Energy* 35 (2010) 1160–1190.
- [4] Y.D. Li, D.X. Li, G.W. Wang, *Catal. Today* 162 (2011) 1–48.
- [5] R.M. Navarro, M.A. Pena, *Chem. Rev.* 107 (2007) 3952–3991.
- [6] Y.D. Li, J.L. Chen, Y.N. Qin, L. Chang, *Energy & Fuel* 14 (2000) 1188–1194.
- [7] S. Takenaka, S. Kobayashi, H. Ogiwara, K. Otsuka, *J. Catal.* 217 (2003) 79–87.
- [8] S. Takenaka, E. Kato, Y. Tomikubo, K. Otsuka, *J. Catal.* 219 (2003) 176–185.
- [9] M.A. Ermakova, D.Y. Ermakov, G.G. Kuvshinov, L.M. Plyasova, *J. Catal.* 187 (1999) 77–84.
- [10] Y. Li, B.C. Zhang, X.L. Tang, Y.D. Xu, W.J. Shen, *Catal. Commun.* 7 (2006) 380–386.
- [11] G.D. Nuernberg, H.V. Fajardo, E.L. Foletto, S.M. Hickel-Probst, N.L.V. Carreno, L.F.D. Probst, J. Barrault, *Catal. Today* 176 (2011) 465–469.
- [12] S. Takenaka, Y. Shigeta, E. Tanabe, K. Otsuka, *J. Catal.* 220 (2003) 468–477.
- [13] A.E. Awadallah, A.A. Aboul-Enein, A.K. Aboul-Gheit, *Renew. Energy* 57 (2013) 671–678.
- [14] N.A. Hermes, M.A. Lansarin, O.W. Perez-Lopez, *Catal. Lett.* 141 (2011) 1018–1025.
- [15] L.B. Avdeeva, O.V. Goncharova, D.I. Kochubey, V.I. Zaikovskii, L.M. Plyasova, B.N. Novgorodov, S.K. Shaikhutdinov, *Appl. Catal. A: Gen.* 141 (1996) 117–129.
- [16] A.R. Naghash, Z. Xu, T.H. Etsell, *Chem. Mater.* 17 (2005) 815–821.
- [17] A. Hornés, P. Beraa, M. Fernández-García, A. Guerrero-Ruizb, A. Martínez-Arias, *Appl. Catal. B: Environ.* 111–112 (2012) 96–105.
- [18] H.Y. Wang, R.T.K. Baker, *J. Phys. Chem. B* 108 (2004) 20273–20277.
- [19] M.J. Lazaro, Y. Echegoyen, I. Suelves, J.M. Palacios, R. Moliner, *Appl. Catal. A: Gen.* 329 (2007) 22–29.
- [20] A.C. Lua, H.Y. Wang, *Appl. Catal. B: Environ.* 132–133 (2013) 469–478.
- [21] T.V. Choudhary, C. Sivadinarayana, C.C. Chusuei, A. Klinghoffer, D.W. Goodman, *J. Catal.* 199 (2001) 9–18.
- [22] H.Y. Wang, A.C. Lua, *J. Phys. Chem. C* 116 (2012) 26765–26775.
- [23] Y. Shen, A.C. Lua, *Sci. Rep.* 3 (2013) 3037.
- [24] T.V. Reshetenko, L.B. Avdeeva, Z.R. Ismagilov, A.L. Chuvilin, V.A. Ushakov, *Appl. Catal. A: Gen.* 247 (2003) 51–63.
- [25] R.T.K. Baker, *Carbon* 27 (1989) 315–323.
- [26] N.M. Rodriguez, M.S. Kim, R.T.K. Baker, *J. Catal.* 140 (1993) 16–29.
- [27] J.L. Chen, X.M. Li, Y.D. Li, Y.N. Qin, *Chem. Lett.* 32 (2003) 424–425.
- [28] J.A. Rodriguez-Manzo, M. Terrones, H. Terrones, H.W. Kroto, L.T. Sun, F. Banhart, *Nat. Nanotechnol.* 2 (2007) 307–311.
- [29] M. Moors, H. Amara, T.V. de Bocarme, C. Bichara, F. Ducastelle, N. Kruse, J.C. Charlier, *ACS Nano* 3 (2009) 511–516.
- [30] S. Helveg, C. Lopez-Cartes, J. Sehested, P.L. Hansen, B.S. Clausen, J.R. Rostrup-Nielsen, F. Abild-Pedersen, J.K. Nørskov, *Nature* 427 (2004) 426–429.
- [31] J.L. Chen, Y.D. Li, Y.M. Ma, Y.N. Qin, L. Chang, *Carbon* 39 (2001) 1467–1475.
- [32] M. Lin, J.P.Y. Tan, C. Boothroyd, K.P. Loh, E.S. Tok, Y.L. Foo, *Nano Lett.* 7 (2007) 2234–2238.
- [33] M. Moseler, F. Cervantes-Sodi, S. Hofmann, G. Csanyi, A.C. Ferrari, *ACS Nano* 4 (2010) 7587–7595.
- [34] Q. Liu, W. Liu, Z.M. Cui, W.G. Song, L.J. Wan, *Carbon* 45 (2007) 268–273.
- [35] M.A. Ermakova, D.Y. Ermakov, A.L. Chuvilin, G.G. Kuvshinov, *J. Catal.* 201 (2001) 183–197.
- [36] M. Monthieux, L. Noe, L. Dussault, J.C. Dupin, N. Latorre, T. Ubieta, E. Romeo, C. Royo, A. Monzon, C. Guimon, *J. Mater. Chem.* 17 (2007) 4611–4618.